

Basic matrix elements for level shifts and widths of hydrogenic levels in ion-surface interactions

P. Kürpick and U. Thumm

J. R. Macdonald Laboratory, Department of Physics, Kansas State University, Manhattan, Kansas 66 506-2604

(Received 11 December 1995; revised manuscript received 15 March 1996)

We present extensive studies of basic one-electron matrix elements involved in ion-metal surface scattering theory. Our method allows for the convenient generation of matrix elements for high principal quantum numbers of hydrogenic projectile states and thus provides basic building blocks for the *ab initio* description of the interaction of highly charged ions with surfaces. The matrix elements related to the energy shifts can be evaluated for an arbitrary one-dimensional potential therefore allowing for flexibility in the choice of model-perturbation potentials. The transfer matrix elements between hydrogenic levels and conduction-band states have been formerly evaluated for the special case of eigenfunctions to the step-function potential. We extend these calculations to wave functions generated from an arbitrary one-dimensional surface potential and show applications to various surface potentials and hydrogenic levels. [S1050-2947(96)02408-0]

PACS number(s): 34.50.Dy, 31.15.-p, 34.70.+e, 61.80.Jh

I. INTRODUCTION

Over the last few decades considerable interest both theoretically and experimentally has been brought to the study of ion-surface scattering processes (for reviews see [1–3]). Early investigations of direct resonance capture at large ion-surface distances and Auger transitions near the surface go back to Hagstrum and Becker [4]. Recent developments of ultrahigh vacuum facilities and the possibility to manufacture extremely flat surfaces allows experimental investigation of the interaction of the ion with the surface in a more controlled manner [5].

From a theoretical point of view several quite different approaches have been undertaken. Level shifts and the broadening of ionic levels induced by the ion-surface interaction have been estimated in first-order approximation by several groups [6–10].

Nonperturbative calculations have been carried out by Burgdörfer and co-workers [2,11,12], Nordlander and Tully [13], Brako and Newns [1], and Teillet-Billy and Gauyacq [14]. Burgdörfer and co-workers used a multichannel theory to investigate the resonant charge transfer. Level shifts and lifetime broadenings were calculated by diagonalizing a self-energy matrix within the $n=2$ manifold. Nordlander and Tully used the complex-rotation technique and large basis sets of generalized Laguerre polynomials up to $n=40$ to diagonalize the time-independent Schrödinger equation. A similar technique has been recently used by Deutscher *et al.* [12,15] to study atomic resonances near an Al surface. Brako and Newns investigated resonant tunneling of electrons between bound ionic or atomic states and the conduction band by means of a model Hamiltonian using the crude assumption that the energy dependence and time dependence separate in the transition matrix elements. Teillet-Billy and Gauyacq developed the coupled-angular-mode method and applied it to evaluate the position and width of the states of a negative ion interacting with a metal surface.

More recently and driven by the experimental investigation of highly charged ions impinging on surfaces, the theoretical description of resonant electron capture into highly excited Rydberg states has become a challenging task. Burg-

dörfer *et al.* [16] have used the classical overbarrier model to investigate both Auger yields and the formation of transient hollow atoms due to resonant charge transfer into Rydberg states.

On a quantum mechanical level no large scale *ab initio* calculation of the full many-electron problem has been performed up to now. An important step toward such a quantum mechanical picture was made by Wille [17–22], who performed a systematic evaluation of one-electron matrix elements between hydrogenic wave functions and eigenfunctions of the step-function potential. He derived exact closed-form expressions for both the overlap and Coulomb matrix element and studied their scaling behavior for large quantum numbers [21].

This work focuses on the analytical and numerical calculation of two types of matrix elements. These basic matrix elements provide the elementary building blocks of a nonperturbative, close-coupling approach to ion-surface interactions. At the same time, they allow perturbative approximations to energy shifts and decay rates of resonance states in front of a metal surface. The first class of matrix elements gives the first-order energy shift of hydrogenic levels due to the interaction with a surface. Even though our approach is restricted to hydrogenic levels, we are able to represent the ion-surface interaction by any model-perturbation potential that is translationally invariant in the surface plane. The second class of matrix elements includes both the overlap and (the possibly modified) Coulomb interaction integrals between hydrogenic projectile states and surface states. These matrix elements have been carefully analyzed by Wille [17–22]. We have generalized the derivation in [17] by allowing for more flexibility in the analytical form of both metal-electron wave function and interaction potential. As special cases, we are able to exactly reproduce the results of Ref. [17]. The analytic evaluation of the matrix elements is done by means of MATHEMATICA [23].

Our paper is structured as follows. In Sec. II, we present a general formalism using channel Hamiltonians which allow us to define the one-electron matrix elements studied later. In Sec. III we give a derivation of one-electron matrix elements involving hydrogenic orbitals and the full metal potential as

they are used in first-order energy shift calculations and evaluations of the self-energy matrix, which includes non-perturbative level shifts and widths [25]. In Secs. IV we derive expressions for the evaluation of one-electron matrix elements involving a hydrogenic wave function and a conduction-band metal state. In Sec. III and IV we show numerical applications for various surface potentials. For the sake of clearness, we have shifted the details involved in the analytical evaluation of the matrix elements to two appendices. Section V contains our conclusions and an outlook to applications of these matrix elements in large scale time-dependent close-coupling calculations. Atomic units (a.u.) are used throughout this paper.

II. CLOSE-COUPPLING FORMALISM FOR ION-SURFACE SCATTERING

Within the independent-particle model the time-dependent single-particle Schrödinger equation for the ion-surface system can be written as

$$\mathcal{H}(\vec{r}, t)\chi(\vec{r}, t) = i \frac{d}{dt} \chi(\vec{r}, t), \quad (2.1)$$

where the Hamiltonian $\mathcal{H}(\vec{r}, t)$ is given by

$$\mathcal{H}(\vec{r}, t) = -\frac{1}{2} \nabla^2 + V_C(\vec{r}, t) + V_{\text{surf}}(\vec{r}) + V_{\text{image}}^N(\vec{r}, t). \quad (2.2)$$

V_C denotes either the bare Coulomb potential of the nucleus for the case of a proton or a state-dependent effective potential for the case of a many-electron ion. In the absence of the projectile, the unperturbed substrate is represented by an effective potential V_{surf} which includes the electronic self-image potential V_{image}^e . V_{image}^N is the image charge potential induced by the projectile nucleus.

To solve the time-dependent equation (2.1), we expand the time-dependent single-particle wave function into two sets of wave functions,

$$\chi(\vec{r}, t) = \sum_j a_j(t) \psi_j(\vec{r}^{\vec{r}}, t) + \int \rho(\vec{k}) b_{\vec{k}}(t) \phi_{\vec{k}}(\vec{r}) d\vec{k}, \quad (2.3)$$

$$\vec{r}^{\vec{r}} = \vec{r} - \vec{R}.$$

Unless otherwise stated, primed coordinates refer to the ion-centered coordinate system and unprimed coordinates refer to the surface-centered coordinate system depicted in Fig. 1.

This basis set is built up by hydrogenic wave functions ψ_j which are eigenfunctions of the stationary Schrödinger equation

$$\left(-\frac{1}{2} \nabla^2 + V_C(\vec{r}^{\vec{r}}) \right) \psi_{nlm}(\vec{r}^{\vec{r}}) = \varepsilon_{nlm} \psi_{nlm}(\vec{r}^{\vec{r}}).$$

For translationally invariant surfaces the conduction-band wave functions are approximated as eigenfunctions of the stationary Schrödinger equation

$$\left(-\frac{1}{2} \nabla^2 + V_{\text{surf}}(z) \right) \phi_{\vec{k}}(\vec{r}) = \varepsilon_k \phi_{\vec{k}}(\vec{r}),$$

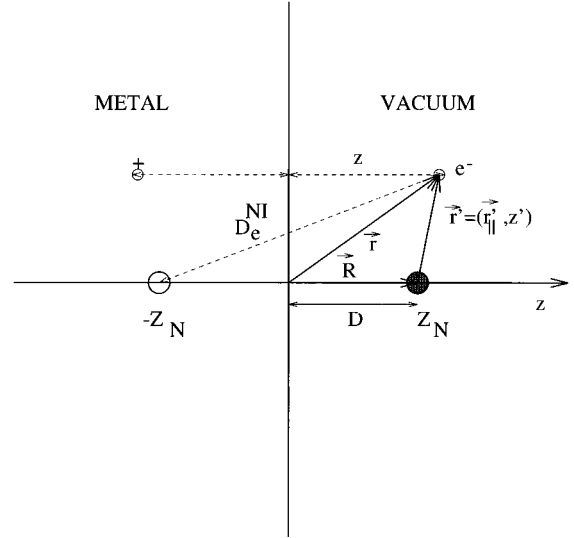


FIG. 1. Ion-metal surface system and coordinates used.

with

$$\phi_{\vec{k}}(\vec{r}) = \frac{1}{\sqrt{V}} \exp(i\vec{k}_{\parallel} \cdot \vec{r}_{\parallel}) g(z).$$

We restrict ourselves to translationally invariant surfaces for which the conduction-band states are plane waves in both the x and y direction. Throughout the paper the normalization is chosen so that $1/\sqrt{V} = 1$.

In order to display how and where one-electron matrix elements are relevant for the *ab initio* treatment of ion-surface interactions at small perpendicular velocities, we now rewrite our initial Hamiltonian (2.2) in terms of entrance and exit channel Hamiltonians [11,24], H_i and H_f , as

$$\mathcal{H} = H_i + V_i = H_f + V_f,$$

with

$$H_i = -\frac{1}{2} \nabla^2 + V_{\text{surf}}, \quad V_i = V_C + V_{\text{image}}^N,$$

and

$$H_f = -\frac{1}{2} \nabla^2 + V_C, \quad V_f = V_{\text{surf}} + V_{\text{image}}^N.$$

Inserting (2.3) into the time-dependent single-particle Schrödinger equation (2.1) and neglecting intraband coupling leads to the close-coupling equations [11]

$$\mathbf{H}^A A(t) = \int d\vec{k} \rho(\vec{k}) M(\vec{k}) b_{\vec{k}}(t), \quad A(t) \equiv \{a_j(t)\} \quad (2.4)$$

$$\left(i \frac{d}{dt} - \varepsilon_k \right) b_{\vec{k}}(t) = M^\dagger(\vec{k}) A(t), \quad (2.5)$$

with

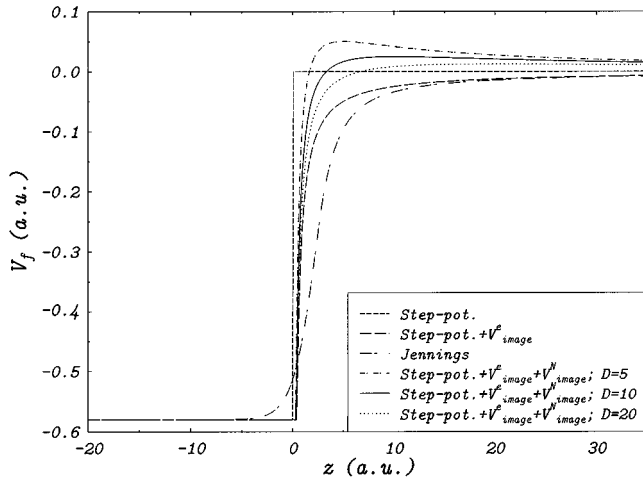


FIG. 2. Potentials used for the FCD matrix elements and ICT matrix elements.

$$H_{jj'}^A = \left(i \frac{d}{dt} - \varepsilon_j \right) \delta_{jj'} - \langle \psi_j | V_f | \psi_{j'} \rangle$$

and

$$M_j(\vec{k}) = \langle \psi_j | \phi_{\vec{k}} \rangle \left(\varepsilon_{\vec{k}} - i \frac{d}{dt} \right) + \langle \psi_j | V_i | \phi_{\vec{k}} \rangle,$$

$$M_j^\dagger(\vec{k}) = \langle \phi_{\vec{k}} | \psi_j \rangle \left(\varepsilon_{\vec{k}} - i \frac{d}{dt} \right) + \langle \phi_{\vec{k}} | V_i | \psi_j \rangle.$$

Depending on the choice of the surface potential the corresponding density of states $\rho(\vec{k})$ has to be used. For the special case of a bare step potential and including a factor 2 for the spin degeneracy, $\rho(\vec{k})$ has the constant value $\rho = V/(4\pi^3)$, or $\rho = 1/(4\pi^3)$ for our normalization of the conduction-band states.

As we will neglect intraband couplings due to the term $\langle \phi_{\vec{k}} | V_i | \phi_{\vec{k}} \rangle$, we are left with two types of basic matrix elements namely, the final channel distortion (FCD) matrix elements, $\langle \psi_j | V_f | \psi_{j'} \rangle$, coupling hydrogenic states through the potential V_f , and the initial channel transfer (ICT) matrix elements $\langle \psi_j | V_i | \phi_{\vec{k}} \rangle$ coupling hydrogenic states to conduction-band states by means of the initial channel distortion potential V_i . In this paper, no attempt will be made to solve the coupled equations (2.4) and (2.5). We will restrict ourselves to the discussion of the properties of the basic matrix elements needed in such a calculation. We plan to use matrix elements in a future work [25] toward the solution of (2.4) and (2.5).

III. FINAL CHANNEL DISTORTION MATRIX ELEMENT

The diagonal matrix elements of the FCD matrix are the first-order perturbative corrections to the level shifts and have been calculated by several authors for the $1s$ and $2s$ states [6,7,9,24]. No systematic analysis, especially for higher quantum numbers and various surface potentials, has been performed up to now.

The evaluation of the FCD matrix element

$$\mathcal{M}_{n,l,m,n',l',m'}^{FCD}(Z_N, D) = \langle \psi_{n,l,m}(\vec{r}) | V_f(z) | \psi_{n',l',m'}(\vec{r}) \rangle \quad (3.1)$$

can be carried out by means of Fourier transformations and use of the residue theorem (see Appendix A). Z_N is the effective nuclear charge of the projectile. D is the ion-surface distance and equal to the z component of \vec{R} . As we have restricted ourselves to final channel distortion potentials V_f which depend only on the coordinate perpendicular to the surface and hydrogenic states, the FCD matrix elements obey the selection rule for the magnetic quantum numbers $m - m' = 0$. Furthermore, the FCD matrix elements are real. We will now discuss the FCD matrix elements for various model potentials collectively plotted in Fig. 2. Details of these potentials are discussed in the subsequent sections.

A. Step potential

We first study level shifts given by the diagonal elements of the FCD matrix (3.1), in the step potential

$$V_f = \begin{cases} -V_0, & z < 0 \\ 0, & z \geq 0 \end{cases} \quad (3.2)$$

neglecting long-range image potential effects. As an example, we took the case of hydrogen impinging on an Al surface therefore choosing the depth of the potential V_0 as 0.58 a.u. This system will be our test system throughout the rest of the paper. Figures 3(a) and 3(b) show the corresponding first-order shifts $\Delta\varepsilon = \langle \psi_{nlm} | V_f | \psi_{nlm} \rangle$ for the $n=4$ and $n=5$ manifolds. The shifts have been plotted versus the ion-surface distance divided by the classical orbital radius $\langle r_n \rangle = n^2/Z_N$. As there is no repulsive part in the potential, all levels are lowered in energy. For each manifold the absolute value of the averaged energy shift increases most rapidly at about $D/\langle r_n \rangle = 1.5, \dots, 2$. This clearly implies a scaling with the mean radius $\langle r_n \rangle$. In previous studies [21] level shifts have been scaled in a similar way with the classical threshold distance $2\langle r_n \rangle$ instead of $\langle r_n \rangle$. As our axis of quantization is the z axis perpendicular to the surface, the low m -quantum number states p_0, d_0, f_0 , etc. have a high probability density towards the surface and are therefore most easily influenced by the surface. In contrast, the high m -quantum number states p_1, d_2, f_3, g_4 , etc. are much less perturbed due to smaller overlap resulting in comparatively small shifts. The offset between these two extreme cases is about 1 in units of $D/\langle r_n \rangle$ and therefore also correlates with the mean radius as depicted in the inset in Fig. 3(b). For higher n (not shown) these scaling properties are more pronounced due to the increasingly classical behavior of hydrogenic states.

B. Step potential and electron image potential

In a second step, we combine the electron image potential and the step potential to the steady total final channel potential

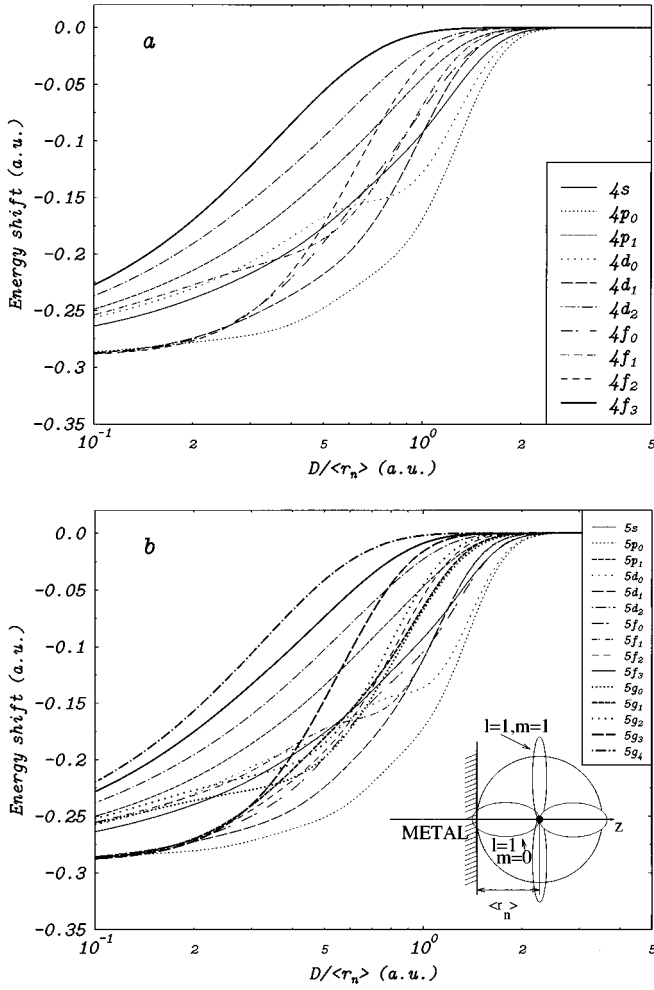


FIG. 3. FCD matrix element for the p -Al ($V_0=0.58$ a.u.) system for the $n=4$ and 5 manifolds. V_f is given by the bare step potential. The inset in (b) gives a schematic view of the ion-surface system and the corresponding low and high m -quantum number states.

$$V_f = \begin{cases} -V_0, & z < \frac{1}{4V_0} \\ -\frac{1}{4z}, & z \geq \frac{1}{4V_0} \end{cases} \quad (3.3)$$

which gives the classical electron self-image potential at large distances from the surface and matches the conduction-band potential at the image plane at $z=1/4V_0$, therefore avoiding the unphysical singularity of the classical self-image potential at $z=0$ (cf. Fig. 2).

Figure 4 shows the resulting energy shifts for the $n=5$ manifold. As the final channel potential V_f now includes the long-range attractive electron image potential, energy shifts become more substantial at larger ion-surface distances than for the step potential. Besides this difference, the approximate $\langle r_n \rangle$ -scaling property with respect to the ion-surface distance found for the step potential is still valid. Furthermore, the ordering of level shifts with respect to the m -quantum number is the same, p_0 , d_0 , f_0 , and g_0 states being perturbed first when the ion approaches the surface.

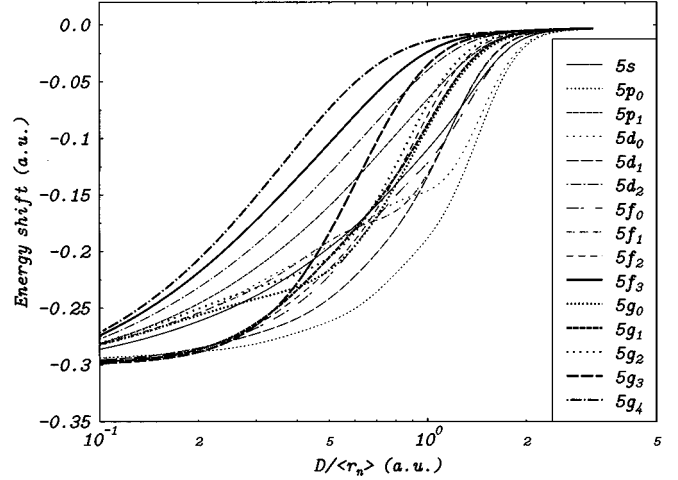


FIG. 4. Same as Fig. 3(b) for the step potential plus electron self-image potential.

The main difference to the bare step potential applies to the $1s$ state (not shown) which is now more drastically disturbed than all other manifolds.

C. *Ab initio* density-functional potential

The former case of the step potential plus the electronic self-image potential should be a crude approximation to any *ab initio* surface potential derived from a more sophisticated density functional approach. To study these differences, we used the potential derived by Jennings, Jones, and Weinert [26]. Jennings, Jones, and Weinert used a full-potential linearized augmented-plane-wave (FLAPW) method to compute effective electronic surface potentials for various metals such as Al, Ni, Cu, and Ag. To actually get a one-dimensional potential they averaged the *ab initio* potential over the surface plane and fitted analytic functions in order to obtain the closed-form expression

$$V_f = \begin{cases} \frac{-V_0}{\mathcal{A} \exp[\mathcal{B}(z-z_0)] + 1}, & z \leq z_0 \\ -\frac{1}{4(z-z_0)} [1 - \exp[-\lambda(z-z_0)]] , & z > z_0 \end{cases} \quad (3.4)$$

with

$$\mathcal{A} = -1 + \frac{4V_0}{\lambda}, \quad \mathcal{B} = \frac{2V_0}{\mathcal{A}}$$

for the surface potential [27].

The Jennings potential (3.4) smoothly interpolates between the conduction-band potential V_0 inside the bulk and the electron self-image potential far outside the surface (cf. Fig. 2). The smearing out is governed by the parameter λ . Additionally, the Jennings potential includes the parameter z_0 which defines the image reference plane. In accordance with Ref. [26] we used $\lambda = 1.0$ a.u. and $z_0 = 2.65$ a.u.

Figure 5 shows the resulting energy shifts for the Jennings potential. Comparing Figs. 4 and 5 one realizes that the changes between the crude potential built up by the step

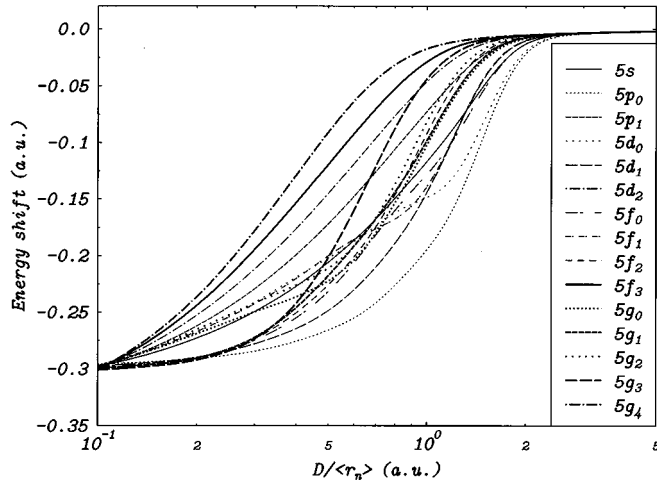


FIG. 5. Same as Fig. 3(b) for the Jennings potential. The Jennings parameters are $\lambda = 1.00$ a.u., $z_0 = 2.65$ a.u.

potential and the electron self-image and the more sophisticated Jennings potential are small. As expected, this statement holds especially at large ion-surface distances, where the two potentials become identical.

D. Step potential, electron, and nuclear image potential

Finally, we consider the case where the repulsive nuclear image potential is taken into account in the final channel potential V_f . The total potential V_f now depends on the ion-surface distance D (cf. Fig. 2) and is given as [9,24]

$$V_f = \begin{cases} -V_0, & z < +R_0 \\ V_{\text{image}} = V_{\text{image}}^e + V_{\text{image}}^N, & z \geq +R_0 \end{cases} \quad (3.5)$$

with

$$R_0 = -\frac{1}{2} \left(D + \frac{Z_N}{V_0} - \frac{1}{4V_0} \right) + \frac{1}{2} \sqrt{\left(D + \frac{Z_N}{V_0} - \frac{1}{4V_0} \right)^2 + \frac{1}{V_0} D}$$

and

$$V_{\text{image}}^e = -\frac{1}{4z}, \quad V_{\text{image}}^N = \frac{Z_N}{D_e^{NI}} \approx \frac{Z_N}{D+z}. \quad (3.6)$$

The classical electron self-image potential unphysically diverges at the surface. We therefore chose the potential to be $-V_0$ for z values below R_0 where the sum of both image potentials matches the bulk value $-V_0$. In addition, we approximated the nuclear image potential by its value on the surface normal through the projectile nucleus [cf. Fig. 1 and Eq. (3.6)]. It should be noted that up to now there has been no easy-to-use potential derived from *ab initio* calculations available for this case of a positive ion in front of a metal surface. Nordlander and Tully [13] derived a nuclear image potential based on the assumption that an ion in front of a metal surface induces a surface charge which changes both the electrostatic field outside the surface and the exchange-

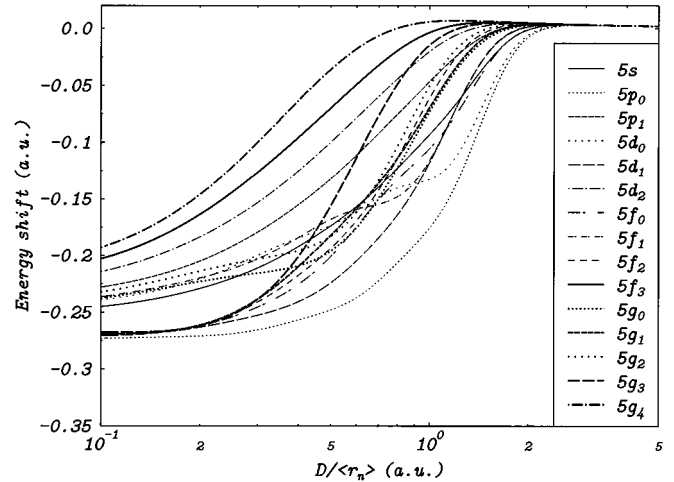


FIG. 6. Same as Fig. 3(b) for the step potential plus both electron self-image potential and nuclear image potential.

correlation potential. These calculations lead to a nuclear image potential which is constant around the point $z = 0$. A similar approach was recently used by Deutscher *et al.* in studies on the adiabatic evolution of the hydrogenic $1s$ state near an aluminum surface [15].

Figure 6 shows the energy shifts using the potential (3.5). For states with a low m -quantum number the energy shift reveals a positive maximum at about 2.0 in units of $D/\langle r_n \rangle$ whereas for high m -quantum numbers this saddle point is at about 1.0. Below these limits all energy shifts drop down to negative values, except for the $1s$ level shift.

To give a better impression of the scaling behavior, Fig. 7 shows the energy shifts for all $n = 1-5$ manifolds on a decadic scale. As for the other three final channel perturbation potentials discussed previously, the $1s$ state does not follow the scaling property of the higher states and is positive for all displayed values of the ion-surface distance D . For all other manifolds one clearly sees the approximate $\langle r_n \rangle$ -scaling be-

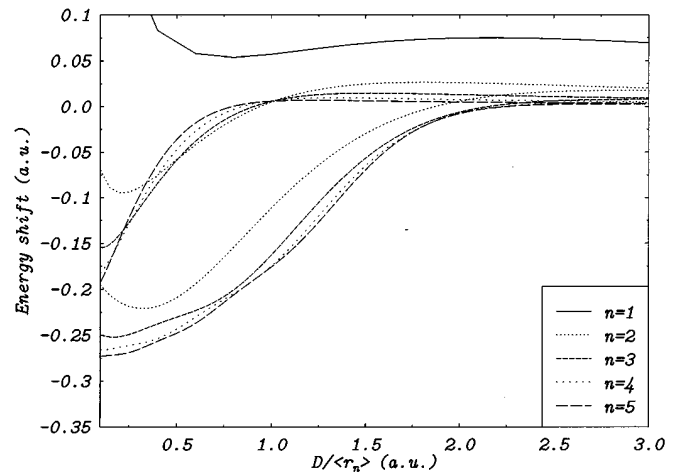


FIG. 7. FCD matrix elements up to $n=5$ shown on a decadic scale for the case of the step potential plus both electron self-image potential and nuclear image potential. Within each n manifold we only show the most easily disturbed p_0 state and the least disturbed ($m=l=n-1$) state.

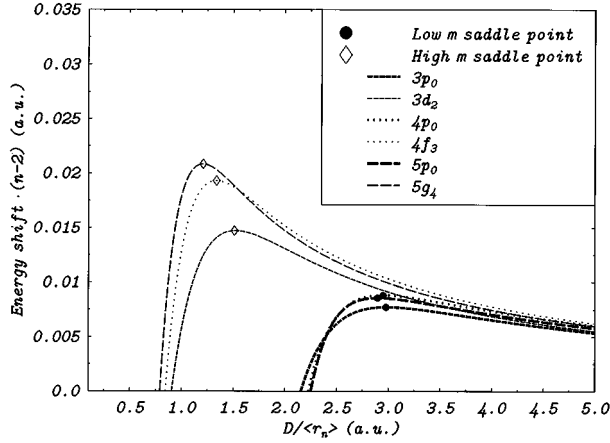


FIG. 8. Energy shifts of low and high m -quantum number states and their corresponding saddle points.

havior with respect to D and the shift by $\langle r_n \rangle$ in the onset for low and high m -quantum number states.

E. Large ion-surface distance high n -quantum number behavior

For the case discussed in Sec. III D above, we have also investigated the behavior of hydrogenic states with high n -quantum numbers at large ion-surface distances. In Fig. 8 we show, focusing on the large ion-surface distance behavior, the energy shifts of the $n=3, \dots, 5$ manifolds for the sets of the most (d_0, f_0, g_0) and the least (d_2, f_3, g_4) disturbed states within each manifold. For ion-surface distances larger than about $4 \langle r_n \rangle$, energy shift reveals a $1/(n-2)$ scaling. We have also marked the saddle points, i.e., the positive maximum of the energy shifts. For the low

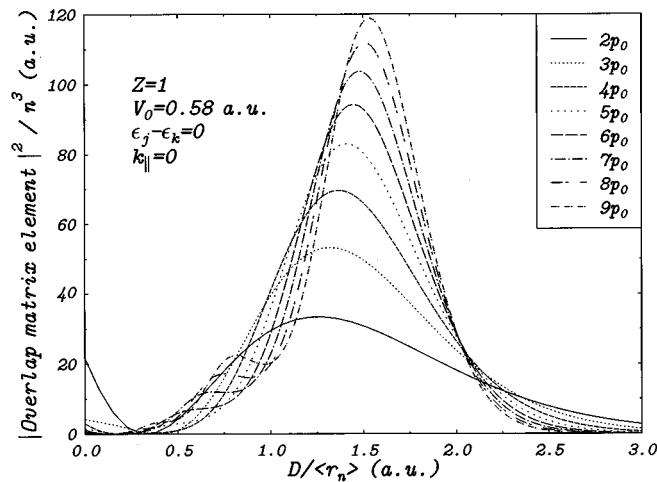


FIG. 9. Square moduli of the overlap matrix elements for the p -Al system for the $2p_0$ to $9p_0$ states. The ion-surface distance was divided by the radial expectation value $\langle r_n \rangle$. The square modulus of each curve was divided by n^3 , n being the main quantum number.

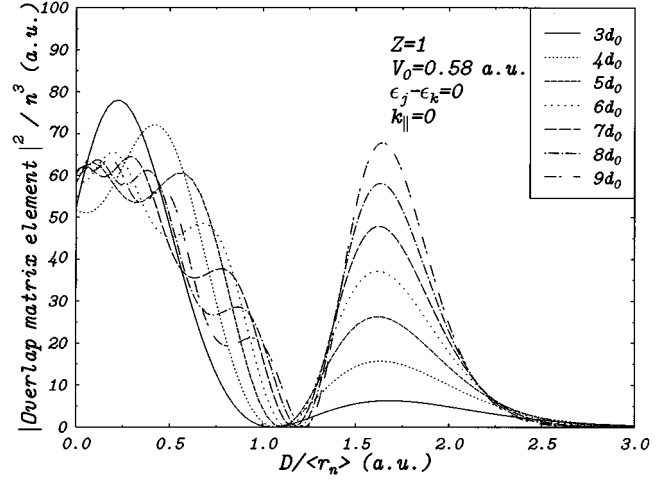


FIG. 10. Same as Fig. 9 for the $3d_0$ to $9d_0$ states.

m -quantum number states its position scales with $\langle r_n \rangle$, whereas for high m -quantum number states it exhibits a slight shift toward small values of $D/\langle r_n \rangle$.

IV. INITIAL CHANNEL TRANSFER MATRIX ELEMENT

ICT matrix elements having the general form

$$\mathcal{M}_{n,l,m}^{\text{ICT}}(\vec{k}; Z_N, D) = \langle \phi_{\vec{k}}(\vec{r}) | V_i | \psi_{n,l,m}(\vec{r}) \rangle \quad (4.1)$$

have recently been studied quite extensively [17–22]. Pioneer work was performed by Wille [17], who derived analytic closed-form expressions for the special case of the overlap matrix element ($V_i=1$) and the Coulomb matrix element ($V_i=-Z_N/|\vec{r}|$), the conduction-band states being approxi-

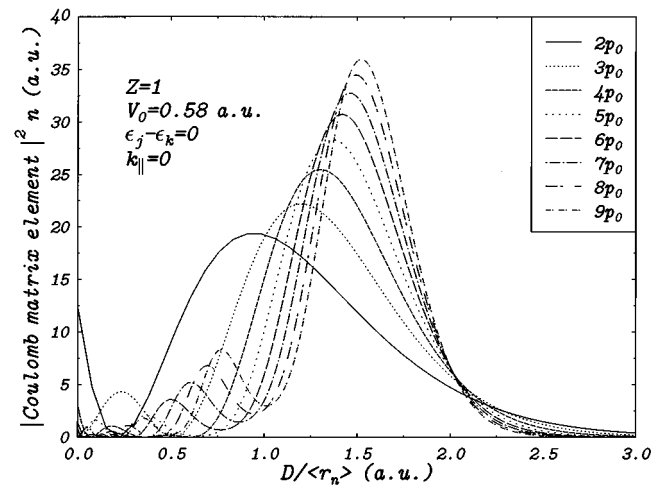


FIG. 11. Square moduli of the Coulomb matrix elements for the p -Al system for the $2p_0$ to $9p_0$ states. As in Fig. 9 the ion-surface distance was divided by $\langle r_n \rangle$, whereas the square modulus of each curve was multiplied by n .

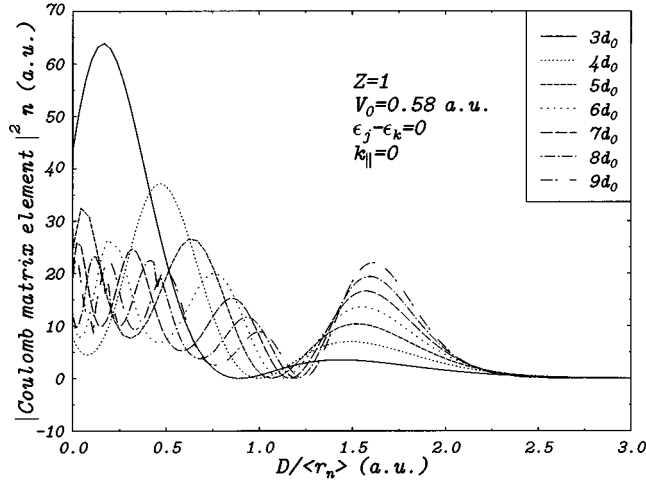


FIG. 12. Same as Fig. 11 for the $3d_0$ to $9d_0$ states.

mated as eigenfunctions of the step-function potential. These analytic expressions, although extremely cumbersome, allow us to calculate the overlap and Coulomb matrix elements for highly excited Rydberg states. These hollow atom states are the primarily populated states of a highly charged ion that approaches a metal surface.

Besides being the basic building blocks for *ab initio* close-coupling calculations, the ICT matrix elements are directly related to the perturbative width

$$\Gamma_{n,l,m}(Z_N, D) = 2\pi \int_{k \leq k_F} d^3k' |\mathcal{M}_{n,l,m}^{\text{ICT}}(\vec{k}'; Z_N, D)|^2 \times \delta(\varepsilon_{nlm} - \varepsilon_{k'}) \rho(\vec{k}').$$

Based on the momentum eigenfunctions as originally derived by Podolsky and Pauling [28] and guided by the work of Thumm [24] and Wille [17], we derived expressions for the more general case of an arbitrary potential $V_i(z)$ and an arbitrary wave function component $g(z)$ along the surface normal. By using Fourier transformations and contour integration, the three-dimensional integral over \vec{r} can be reduced to a one-dimensional integral along the surface normal. For the sake of clearness, we shifted the details of the evaluation of the ICT matrix elements to Appendix B. Furthermore, we will not attempt an extensive discussion of scaling properties as done by Wille [21] for the special case of the step-potential eigenstates and ($l=0$) states on the projectile, but restrict ourselves to obvious scaling properties occurring for l -quantum numbers up to $l=2$.

Our numerical results agree to the tenth digit with those of Wille [29]. As an example, Figs. 9–12 show the square moduli of the overlap and Coulomb matrix element for the p and d states up to $n=9$ and an aluminum surface. In all cases we set $k_{||}=0$ and chose k_z so as to have the energetically resonant case which implies that only the ($m=0$) matrix elements are nonzero. Both types of matrix elements exhibit for all l -quantum numbers an $\langle r_n \rangle$ -scaling behavior with respect to the ion-surface distance which reflects the

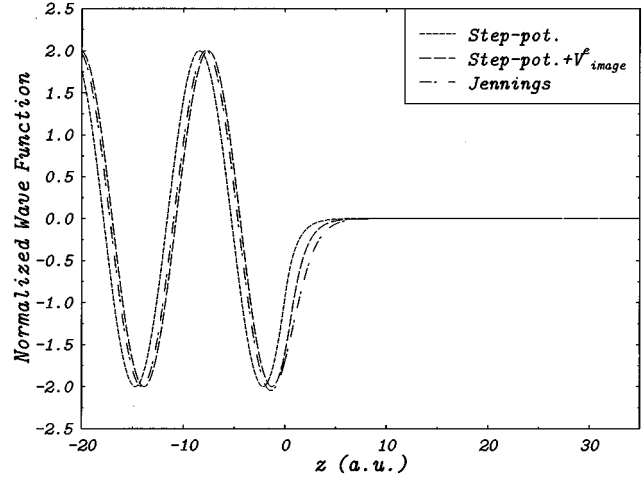


FIG. 13. Conduction-band wave functions for the case of $k_{||}=0$ and $k_z=0.50$ for three of the potentials shown in Fig. 2.

classical behavior of high n -quantum number states. The function values of the square moduli of the matrix elements scale very differently. The square modulus of the overlap matrix element reveals an n^3 scaling whereas the Coulomb matrix element scales with $1/n$. The implied $1/n^2$ scaling of the ratio

$$\mathcal{R} = \frac{\langle \phi_{\vec{k}}(\vec{r}) | V_C | \psi_{n,l,m}(\vec{r}^{\vec{T}}) \rangle}{\langle \phi_{\vec{k}}(\vec{r}) | \psi_{n,l,m}(\vec{r}^{\vec{T}}) \rangle} = \frac{-Z_N^2}{n^2} + \frac{\left\langle \phi_{\vec{k}}(\vec{r}) \left| \frac{\nabla^2}{2} \right| \psi_{n,l,m}(\vec{r}^{\vec{T}}) \right\rangle}{\langle \phi_{\vec{k}}(\vec{r}) | \psi_{n,l,m}(\vec{r}^{\vec{T}}) \rangle}$$

can be easily understood as the last term on the right side approximately vanishes for high n -quantum numbers.

Comparison of various surface potentials

We now investigate the sensitivity of the ICT matrix element and overlap integrals on $V_i(z)$ and the wave function component perpendicular to the surface, $g(z)$. We consistently use wave functions $g(z)$ that are eigenfunctions to $V_i(z)$. Except for the step potential, we numerically generated $g(z)$.

Figure 13 presents the eigenstates for the case of $k_{||}=0$ and $k_z=0.50$ for the three surface potentials studied (cf. Fig. 2). Besides the bare step potential, we studied the step potential plus the electron self-image potential and the Jennings potential as defined in Eq. (3.4). At large ion-surface distances the Jennings potential matches the classical electron self-image potential, whereas below 10 a.u. it shows significant deviations from the former. The Jennings potential reaches its bulk value of $V_0=0.58$ only as deep as 5 a.u. inside the surface. This clearly influences the corresponding wave function. Jennings states with energies below $-V_0/\{\text{Aexp}[\mathcal{B}(z_0)]+1\}$ are less emanating from the surface, whereas those having higher energies reach far more outside the surface than step-potential eigenstates. A close

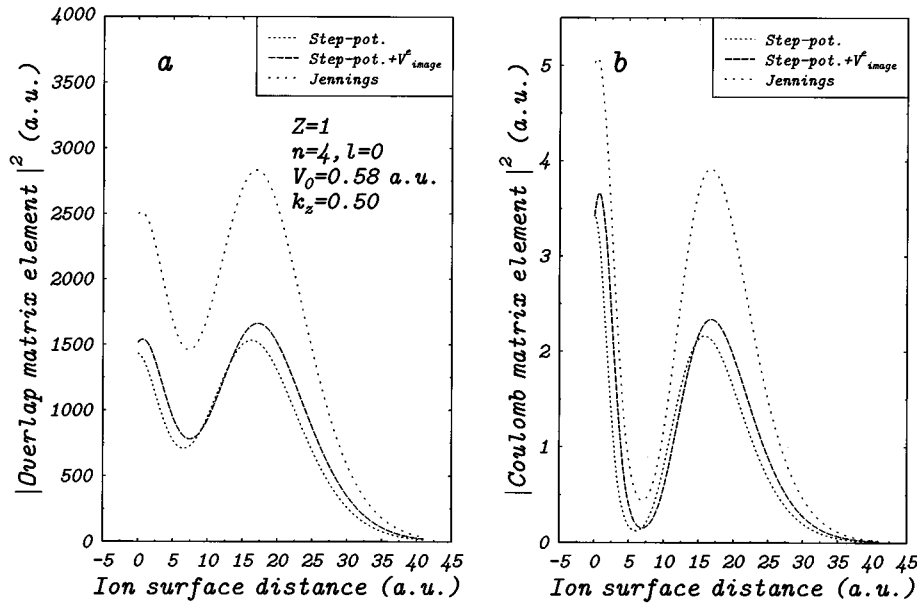


FIG. 14. Overlap (a) and Coulomb matrix elements (b) of the $4s$ state for the p -Al system for the bare step potential, the step potential plus the electron self-image potential, and the Jennings potential.

look at the wave functions presented in Fig. 13 reveals that although all three wave functions reach the same wavelength inside the bulk, the Jennings wave function has a slightly bigger wavelength and a larger maximum amplitude at the surface. The Jennings wave function was normalized so as to asymptotically ($z \rightarrow -\infty$) match the step-potential wave function in amplitude.

The influence of the different potentials upon the overlap and Coulomb matrix element can be seen in Fig. 14. As an example, we have calculated the overlap and Coulomb matrix element for the $4s$ state and selected the conduction-band wave function for the non-resonant case $k_z = 0.50$ and $k_{\parallel} = 0$. The two types of matrix elements behave very similarly for the case of the bare step potential and the step potential plus the electronic self-image potential. In contrast to these two former potentials, the Jennings potential gives matrix elements which are remarkably different. We note that the strongly enhanced outermost maximum of both matrix elements and overlaps for the Jennings potential needs to be correlated with the normalization of the metal wave functions. In all measurable quantities, this enhancement may get modified as matrix elements and overlaps are weighted with appropriate density-of-states functions.

V. CONCLUSION

We have presented an extensive study of basic matrix elements for ion-surface interactions. Our method allows for the convenient generation of matrix elements for high principle quantum numbers of the projectile states and thus provides basic building blocks for the *ab initio* description of highly charged ion-surface interactions.

The final channel distortion matrix element involving hydrogenic states of the ion and the initial channel transfer matrix element involving a conduction-band state and a hydrogenic state have been studied for various interaction potentials. Both types of matrix elements scale with respect to the ion-surface distance D divided by the classical radius

$\langle r_n \rangle$. This scaling property holds especially well for high n -quantum number states. For the magnitude of the FCD matrix elements and the case of the full metal potential including the electronic and nuclear image potential, we derived additional scaling properties at large ion-surface distances.

For the ICT matrix elements the former results of Wille [17] have been confirmed. In addition, these matrix elements have been compared for three types of model surface potentials. Although the Jennings potential showed small deviations from the bare step potential plus the electron self-image potential for the FCD matrix elements, its deviations are rather large for the ICT matrix elements. Further investigations are needed to study the influence of these dramatic changes upon the lifetime broadening and energy shifts. Nonperturbative calculations of the self-energy based upon these matrix elements are in progress [25].

ACKNOWLEDGMENTS

This work was supported by the Division of Chemical Sciences, Basic Energy Sciences, Office of Energy Research, U.S. Department of Energy and the Deutsche Forschungsgemeinschaft (DFG) through a grant for P.K. We thank U. Wille for many fruitful discussions.

APPENDIX A: EVALUATION OF FCD MATRIX ELEMENTS

We derive a one-dimensional integral for the hydrogenic one-electron matrix elements involving a potential depending on the electronic coordinate along the axis of quantization (for the sake of clarity we use \vec{r} instead of $r^{\vec{r}}$):

$$\mathcal{M}_{n,l,m,n',l',m'}^{\text{FCD}}(Z_N, D) = \langle \psi_{n,l,m}(\vec{r}) | V(z) | \psi_{n',l',m'}(\vec{r}) \rangle.$$

The general matrix element [30]

$$\begin{aligned}
\mathcal{M}_{n,l,m,n',l',m'}^{\text{FCD}}(Z_N, D) &= \int d\vec{r} R_{nl}^*(r) \mathcal{Y}_{lm}^*(\theta, \phi) V(z) R_{n'l'}(r) \mathcal{Y}_{l'm'}(\theta, \phi) \\
&= \frac{4(2^{l+l'})(Z_N/n)^{3/2+l}(Z_N/n')^{3/2+l'} \sqrt{(l+n)!/n(-1-l+n)!} \sqrt{(l'+n')!/n'(-1-l'+n')!}}{(1+2l)!(1+2l')!} \\
&\quad \times \int dr r^{l+l'} e^{-Fr} V(z) {}_1F_1\left(1+l-n, 2+2l, \frac{2rZ_N}{n}\right) {}_1F_1\left(1+l'-n', 2+2l', \frac{2rZ_N}{n'}\right) \\
&\quad \times \mathcal{Y}_{lm}^*(\theta, \phi) \mathcal{Y}_{l'm'}(\theta, \phi),
\end{aligned}$$

with

$$F = \frac{Z_N}{n} + \frac{Z_N}{n'}$$

is *nonzero* only if $m = m'$, by eliminating the ϕ dependence. It satisfies $\mathcal{M}_{n,l,m,n',l',m'}^{\text{FCD}}(Z_N, D) = \mathcal{M}_{n,l,-m,n',l',-m'}^{\text{FCD}}(Z_N, D)$. The matrix element is *real* and can be calculated in a straightforward way by means of MATHEMATICA [23]. The actual integration is now done in Cartesian coordinates using the fact that $\cos(\theta) = z/r$. This allows the product of spherical harmonics $\mathcal{Y}_{lm}^*(\theta, \phi) \mathcal{Y}_{l'm'}(\theta, \phi)$ to be written in terms of a polynomial in z/r . The matrix element can therefore be rewritten as

$$\begin{aligned}
\mathcal{M}_{n,l,m,n',l',m'}^{\text{FCD}}(Z_N, D) &= \mathcal{N}(n, n', l, l', Z_N) \int dx dy dz V(z) \\
&\quad \times \underbrace{(A_0 + A_1 r^1 + A_2 r^2 + \dots + A_\nu r^\nu)}_{r^{l+l'} {}_1F_1(1+l-n, 2+2l, 2rZ_N/n) {}_1F_1(1+l'-n', 2+2l', 2rZ_N/n')} \\
&\quad \times \underbrace{\left[B_0 + B_1 \left(\frac{z}{r}\right)^1 + B_2 \left(\frac{z}{r}\right)^2 + \dots + B_\mu \left(\frac{z}{r}\right)^\mu \right]}_{\mathcal{Y}_{lm}^*(\theta, \phi) \mathcal{Y}_{l'm'}(\theta, \phi)} \\
&\quad \times e^{-Fr},
\end{aligned}$$

with

$$\mathcal{N}(n, n', l, l', Z_N) = \frac{4(2^{l+l'})(Z_N/n)^{3/2+l}(Z_N/n')^{3/2+l'} \sqrt{(l+n)!/n(-1-l+n)!} \sqrt{(l'+n')!/n'(-1-l'+n')!}}{(1+2l)!(1+2l')!}$$

Expanding the polynomials one gets

$$\mathcal{M}_{n,l,m,n',l',m'}^{\text{FCD}}(Z_N, D) = \mathcal{N}(n, n', l, l', Z_N) \int dx dy dz V(z) (C_{-\mu} r^{-\mu} + C_{-\mu+1} r^{-\mu+1} + \dots + C_\eta r^\eta) e^{-Fr},$$

where the coefficients $C_{-\mu}, C_{-\mu+1}, \dots, C_\eta$ depend on z .

We now use the Fourier transformation

$$r^n e^{-Fr} = \underbrace{\int \frac{1}{4\pi^2} (n+1)! \frac{1}{ik} \left[\frac{(F+ik)^{n+2} - (F-ik)^{n+2}}{(F^2+k^2)^{n+2}} \right]}_{\mathcal{F}(\vec{k}, n)} \exp(i\vec{k} \cdot \vec{r}) d\vec{k}$$

and obtain

$$\begin{aligned}
\mathcal{M}_{n,l,m,n',l',m'}^{\text{FCD}}(Z_N, D) &= \mathcal{N}(n, n', l, l', Z_N) \int dx dy dz V(z) \left(C_{-\mu} \int \mathcal{F}(\vec{k}, -\mu) \exp(i\vec{k} \cdot \vec{r}) d\vec{k} \right. \\
&\quad \left. + C_{-\mu+1} \int \mathcal{F}(\vec{k}, -\mu+1) \exp(i\vec{k} \cdot \vec{r}) d\vec{k} + \dots + C_\eta \int \mathcal{F}(\vec{k}, \eta) \exp(i\vec{k} \cdot \vec{r}) d\vec{k} \right).
\end{aligned}$$

Interchanging the integration over \vec{r} and \vec{k} we get

$$\begin{aligned} \mathcal{M}_{n,l,m,n',l',m'}^{\text{FCD}}(Z_N, D) = & \mathcal{N}(n, n', l, l', Z_N) \int dz V(z) \left(C_{-\mu} \int d\vec{k} \int dx \int dy \exp(ik_x x) \exp(ik_y y) \mathcal{F}(\vec{k}, -\mu) \exp(ik_z z) \right. \\ & + \underbrace{C_{-\mu+1} \int d\vec{k} \int dx \int dy \exp(ik_x x) \exp(ik_y y) \mathcal{F}(\vec{k}, -\mu+1) \exp(ik_z z)}_{(2\pi)^2 \delta(k_x) \delta(k_y)} + \dots \\ & \left. + C_\eta \int d\vec{k} \int dx \int dy \exp(ik_x x) \exp(ik_y y) \mathcal{F}(\vec{k}, \eta) \exp(ik_z z) \right). \end{aligned}$$

This reduces the matrix element to

$$\begin{aligned} \mathcal{M}_{n,l,m,n',l',m'}^{\text{FCD}}(Z_N, D) = & (2\pi)^2 \mathcal{N}(n, n', l, l', Z_N) \int dz V(z) \left(C_{-\mu} \int dk_z \mathcal{F}(k_z, -\mu) \exp(ik_z z) \right. \\ & \left. + C_{-\mu+1} \int dk_z \mathcal{F}(k_z, -\mu+1) \exp(ik_z z) + \dots + C_\eta \int dk_z \mathcal{F}(k_z, \eta) \exp(ik_z z) \right). \end{aligned}$$

Now, each of the terms $\int dk_z \mathcal{F}(k_z, \eta) \exp(ik_z z)$ can be evaluated by means of the residue theorem. Depending on the sign of z we get

$$\int dk_z \mathcal{F}(k_z, \eta) \exp(ik_z z) = \begin{cases} 2\pi i \text{Res}(\mathcal{F}(k_z, \eta) \exp(ik_z z); k_z = iF), & z \geq 0 \\ -2\pi i \text{Res}(\mathcal{F}(k_z, \eta) \exp(ik_z z); k_z = -iF), & z < 0. \end{cases}$$

APPENDIX B: EVALUATION OF ICT MATRIX ELEMENTS

We derive a one-dimensional integral for the transfer matrix element involving an arbitrary hydrogenic wave function and a conduction-band state. $V(z)$ is any potential that depends only on the z coordinate perpendicular to the surface. We follow the notation of Wille [17].

$$\mathcal{M}_{n,l,m}^{\text{ICT}}(\vec{k}; Z_N, D) = \langle \phi_{\vec{k}}(\vec{r}) | V(z) | \psi_{nlm}(\vec{r}^\vec{T}) \rangle,$$

with

$$\vec{r}^\vec{T} = \vec{r} - \vec{R}.$$

1. Definition of the conduction-band wave function

Restricting ourselves to the case of plane-wave states in both the x and y direction, conduction-band wave functions have the general form (using $1/\sqrt{V}=1$)

$$\phi_{\vec{k}}(\vec{r}) = \exp(ik_x x) \exp(ik_y y) g_{k_z}(z).$$

A density of states that is consistent with the choice of $g_{k_z}(z)$ needs to be taken into account when matrix elements are integrated over \vec{k} .

2. Definition of hydrogenic wave functions in momentum space

We use the Fourier transform

$$\tilde{f}(\vec{q}) = \tilde{\psi}_{nlm}(\vec{q}) = (-i)^l \tilde{\mathcal{R}}_{nl}(\vec{q}) \mathcal{Y}_l^m(\theta_q, \phi_q) \quad (\text{B1})$$

of the hydrogenic wave function, including a translational factor to guarantee Galilei invariance (cf. [31]),

$$f(\vec{r}^\vec{T}) = \psi_{nlm}(\vec{r}^\vec{T}),$$

$$f(\vec{r}) = \frac{1}{(2\pi)^{3/2}} \int_{-\infty}^{\infty} d\vec{q} \exp[i(\vec{q} + \vec{v}) \cdot \vec{r} - iDq_z] \tilde{f}(\vec{q})$$

as originally derived by Podolsky and Pauling [28] (see also [32,17]). Note that we allow for $\vec{v} \neq 0$, whereas in all numerical examples we considered the static limit ($\vec{v}=0$).

3. Reduction of the three-dimensional integral

We reduce the general three-dimensional integral over \vec{r} by exploiting the plane-wave behavior of the conduction-band states with respect to the x and y directions,

$$\begin{aligned} \mathcal{M}_{n,l,m}^{\text{ICT}}(\vec{k}; Z_N, D) &= \frac{1}{(2\pi)^{3/2}} \int_{-\infty}^{\infty} dz \int_{-\infty}^{\infty} dx \int_{-\infty}^{\infty} dy \exp(-ik_x x) \exp(-ik_y y) \int d\vec{q} \exp[i(\vec{q} + \vec{v}) \cdot \vec{r} - iDq_z] \tilde{f}(\vec{q}) g_{k_z}^*(z) V(z) \\ &= \sqrt{2\pi} \int_{-\infty}^{\infty} dz \exp(iv_z z) g_{k_z}^*(z) V(z) \underbrace{\int_{-\infty}^{\infty} dq_z \tilde{f}(q_z; k'_x, k'_y) \exp[iq_z(z-D)]}_{F(q_z)}, \end{aligned}$$

where

$$k'_x = k_x - v_x, \quad k'_y = k_y - v_y.$$

$$\mathcal{Q}_{lm} := \tilde{N}_{lm} (q_z^2 + k_{\parallel}^{\prime 2})^{l/2} P_l^m \left(\frac{q_z}{\sqrt{q_z^2 + k_{\parallel}^{\prime 2}}} \right) \exp(im\phi_{k'}),$$

4. Evaluation of one-dimensional momentum integration

We introduce the following abbreviations [17]:

$$\tilde{N}_{lm} := (-1)^m \sqrt{\frac{(2l+1)(l-m)!}{4\pi(l+m)!}},$$

$$F(q_z) := \frac{\mathcal{F}_1(q_z)}{(q_z^2 + k_+^{\prime 2})^{n+1}} = \frac{\mathcal{F}_1(q_z)}{(q_z - ik_+^{\prime})^{n+1} [q_z - (-ik_+^{\prime})]^{n+1}}, \quad \text{and}$$

$$\mathcal{F}_1(q_z) := (-i)^l \mathcal{P}_{nl}(q_z) \mathcal{Q}_{lm}(q_z),$$

$$\mathcal{P}_{nl}(q_z) := N_{nl} (q_z^2 + k_+^{\prime 2})^{n-l-1} \mathcal{C}_{n-l-1}^{l+1} \left(\frac{q_z^2 + k_-^{\prime 2}}{q_z^2 + k_+^{\prime 2}} \right),$$

$$\tan(\phi_{k'}) = \frac{k'_y}{k'_x},$$

$$N_{nl} := \sqrt{\frac{2n(n-l-1)!}{\pi(n+l)!}} 2^{2(l+1)} l! \kappa_n^{l+5/2},$$

$$k_+^{\prime 2} := \sqrt{k_{\parallel}^{\prime 2} + \kappa_n^2}, \quad k_-^{\prime 2} := k_{\parallel}^{\prime 2} - \kappa_n^2.$$

$$\kappa_n = \frac{Z}{n} \equiv \sqrt{-2\varepsilon_n}$$

$\mathcal{C}_{n-l-1}^{l+1}$ are Gegenbauer polynomials and P_l^m are associated Legendre polynomials. The transfer matrix element can now be rewritten as

$$\begin{aligned} \mathcal{M}_{n,l,m}^{\text{ICT}}(\vec{k}; Z_N, D) &= (-i)^l \sqrt{2\pi} \exp(im\phi_{k'}) N_{nl} \tilde{N}_{lm} \int_{-\infty}^{\infty} dz' \exp(iv_z z) g_{k_z}^*(z) V(z) \int_{-\infty}^{\infty} dq_z (q_z^2 + k_+^{\prime 2})^{n-l-1} \\ &\quad \times (q_z^2 + k_{\parallel}^{\prime 2})^{l/2} \mathcal{C}_{n-l-1}^{l+1} \left(\frac{q_z^2 + k_-^{\prime 2}}{q_z^2 + k_+^{\prime 2}} \right) P_l^m \left(\frac{q_z}{\sqrt{q_z^2 + k_{\parallel}^{\prime 2}}} \right) \frac{\exp(iq_z z')}{(q_z - ik_+^{\prime})^{n+1} [q_z - (-ik_+^{\prime})]^{n+1}}, \end{aligned}$$

with

$$z' = z - D.$$

The actual calculation of the complex q_z integral is done analytically by using the MATHEMATICA package [23]. We therefore rewrite the transfer matrix element in a more compact form which enables both MATHEMATICA to handle as few terms as possible and gives easy control of the results. We define

$$\mathcal{A}(n, l, m, \phi_{k'}) = (-i)^l \sqrt{2\pi} \exp(im\phi_{k'}) N_{nl} \tilde{N}_{lm},$$

$$\begin{aligned} \mathcal{I}(n, l, m, q_z, z') &= (q_z^2 + k_+^{\prime 2})^{n-l-1} (q_z^2 + k_{\parallel}^{\prime 2})^{l/2} \mathcal{C}_{n-l-1}^{l+1} \left(\frac{q_z^2 + k_-^{\prime 2}}{q_z^2 + k_+^{\prime 2}} \right) P_l^m \left(\frac{q_z}{\sqrt{q_z^2 + k_{\parallel}^{\prime 2}}} \right) \\ &\quad \times \frac{\exp(iq_z z')}{(q_z - ik_+^{\prime})^{n+1} [q_z - (-ik_+^{\prime})]^{n+1}}. \end{aligned} \quad (\text{B3})$$

The transfer matrix element can now be written as

$$\mathcal{M}_{n,l,m}^{\text{ICT}}(\vec{k}; Z_N, D) = \mathcal{A}(n, l, m, \phi_{k'}) \int_{-\infty}^{\infty} dz' \exp(iv_z z) V(z) \begin{cases} g_{k_z}^*(z) (-2\pi i) \text{Res}(\mathcal{I}(n, l, m, q_z, z'); q_z = +ik'_+), & z' < -D \\ g_{k_z}^*(z) (-2\pi i) \text{Res}(\mathcal{I}(n, l, m, q_z, z'); q_z = -ik'_+), & -D \leq z' < 0 \\ g_{k_z}^*(z) (+2\pi i) \text{Res}(\mathcal{I}(n, l, m, q_z, z'); q_z = +ik'_+), & z' \geq 0 \end{cases} \quad (\text{B4})$$

where $z' = z - D$.

5. Calculation of transfer matrix elements involving the product of the Coulomb potential and an arbitrary screening function

For the special case of the transfer matrix element involving an arbitrary hydrogenic wave function, a conduction-band state, the radial Coulomb potential, and an anisotropic screening function $h(z)$,

$$\mathcal{M}_{n,l,m}^{\text{ICT}}(\vec{k}; Z_N, D) = \langle \phi_{\vec{k}}(\vec{r}) | V_C(r') h(z) | \psi_{nlm}(\vec{r}^{\vec{T}}) \rangle,$$

with

$$\vec{r}^{\vec{T}} = \vec{r} - \vec{R}$$

can be calculated by using the same procedure.

Instead of using the Fourier transform of the bare hydrogenic wave function as defined in Eq. (B1), we now use the Fourier transform

$$\tilde{f}(\vec{q}) = \tilde{\psi}_{nlm}(\vec{q}) = -\frac{1}{2} (q^2 + \kappa_n^2) (-i)^l \tilde{\mathcal{R}}_{nl}(q) \mathcal{Y}_l^m(\theta_q, \phi_q)$$

of

$$f(\vec{r}^{\vec{T}}) = -\frac{Z}{r^{\vec{T}}} \psi_{nlm}(\vec{r}^{\vec{T}}), f(r) = \frac{1}{(2\pi)^{3/2}} \int_{-\infty}^{\infty} d\vec{q} \times \exp[i(\vec{q} + \vec{v}) \cdot \vec{r}' - iDq_z] \tilde{f}(\vec{q}).$$

The derivation is unchanged down to Eq. (B2). Now we use the abbreviations [17]

$$F(q_z) := \frac{\mathcal{F}_2(q_z)}{(q_z^2 + k'_+{}^2)^n} = \frac{\mathcal{F}_2(q_z)}{(q_z - ik'_+)^n [q_z - (-ik'_+)]^n},$$

$$\mathcal{F}_2(q_z) := -\frac{1}{2} (-i)^l \mathcal{P}_{nl}(q_z) \mathcal{Q}_{lm}(q_z).$$

As a result $\mathcal{I}(n, l, m, q_z, z')$ is changed to [cf. (B3)]

$$\mathcal{I}(n, l, m, q_z, z') = -\frac{1}{2} (q_z^2 + k'_+{}^2)^{n-l-1} (q_z^2 + k'_+{}^2)^{l/2} C_{n-l-1}^{l+1} \times \left(\frac{q_z^2 + k'_+{}^2}{q_z^2 + k'_+{}^2} \right) P_l^m \left(\frac{q_z}{\sqrt{q_z^2 + k'_+{}^2}} \right) \times \frac{\exp(iq_z z')}{(q_z - ik'_+)^n [q_z - (-ik'_+)]^n}$$

and $V(z)$ becomes $h(z)$ in Eq. (B4).

-
- [1] R. Brako and D. M. Newns, Rep. Prog. Phys. **52**, 655 (1989).
 [2] J. Burgdörfer, in *Review of Fundamental Processes and Applications of Atoms and Ions*, edited by C. D. Lin (World Scientific, Singapore, 1993), p. 517.
 [3] H. Niehus, W. Heiland, and E. Taglauer, Surf. Sci. Rep. **17**, 213 (1993).
 [4] H. D. Hagstrum and G. E. Becker, Phys. Rev. B **8**, 107 (1973).
 [5] H. Winter, Comments At. Mol. Phys. **26**, 287 (1991).
 [6] J. W. Gadzuk, Surf. Sci. **6**, 133 (1967).
 [7] J. W. Gadzuk, Surf. Sci. **6**, 159 (1966). [Equation (20) in this work by Gadzuk is too small by a factor of 2 and therefore the corresponding shifts should be corrected.]
 [8] B. A. Trubnikov and Yu. N. Yavlinskii, Zh. Éksp. Teor. Fiz. **52**, 1638 (1967) [Sov. Phys. JETP **25**, 1089 (1967)].
 [9] M. Remy, J. Chem. Phys. **53**, 2487 (1970).
 [10] A. G. Borisov and U. Wille, Surf. Sci. **338**, L875 (1995).
 [11] J. Burgdörfer, E. Kupfer, and H. Gabriel, Phys. Rev. A **36**, 4963 (1987).
 [12] S. Deutscher, X. Yang, and J. Burgdörfer, Nucl. Instrum. Methods B **100**, 336 (1995).
 [13] P. Nordlander and J. C. Tully, Phys. Rev. B **42**, 5564 (1990).
 [14] D. Teillet-Billy and J. P. Gauyacq, Surf. Sci. **239**, 343 (1990).
 [15] S. Deutscher, X. Yang, J. Burgdörfer, and H. Gabriel (unpublished).
 [16] J. Burgdörfer, P. Lerner, and F. W. Meyer, Phys. Rev. A **42**, 5674 (1991).
 [17] U. Wille, Phys. Rev. A **45**, 3002 (1992).
 [18] U. Wille, Nucl. Instrum. Methods B **67**, 132 (1992).
 [19] U. Wille, Nucl. Instrum. Methods B **90**, 295 (1994).
 [20] U. Wille, Surf. Sci. **307-309**, 874 (1994).
 [21] U. Wille, Phys. Rev. B **50**, 1888 (1994).
 [22] U. Wille, Nucl. Instrum. Methods B **100**, 303 (1995).
 [23] S. Wolfram, *Mathematica, A System for Doing Mathematics by Computer* (Addison-Wesley, Reading, MA, 1993).
 [24] U. Thumm, Ph.D. thesis, Universität Freiburg, 1989.
 [25] P. Kürpick and U. Thumm (unpublished).

- [26] P. J. Jennings, R. O. Jones, and M. Weinert, *Phys. Rev. B* **37**, 6113 (1988).
- [27] We note that Jennings *et al.* have chosen their coordinate system so as to have negative z values outside the surface and used Rydberg atomic units.
- [28] B. Podolsky and L. Pauling, *Phys. Rev.* **34**, 109 (1929).
- [29] U. Wille (private communication).
- [30] A. S. Davydov, *Quantum Mechanics* (Pergamon Press, New York, 1965), p. 138.
- [31] U. Thumm and J. Briggs, *Nucl. Instrum. Methods B* **43**, 471 (1989).
- [32] H. A. Bethe and E. E. Salpeter, in *Handbüch der Physik*, edited by S. Flügge (Springer, Berlin, 1957), p. 88.